IOP Publishing Quantum Sci. Technol. 8 (2023) 025012 https://doi.org/10.1088/2058-9565/acba40

Quantum Science and Technology

OPEN ACCESS

RECEIVED
7 September 2022

REVISED
26 January 2023

ACCEPTED FOR PUBLICATION
8 February 2023

PUBLISHED
17 February 2023

PAPER

A strain-engineered graphene qubit in a nanobubble

Hee Chul Park[1,2], **JungYun Han**[1] **and Nojoon Myoung**[3,*]

[1] Center for Theoretical Physics of Complex Systems, Institute for Basic Science, Daejeon 34051, Republic of Korea
[2] Department of Physics, Pukyong National University, Busan 48513, Republic of Korea
[3] Department of Physics Education, Chosun University, Gwangju 61452, Republic of Korea
[*] Author to whom any correspondence should be addressed.

E-mail: nmyoung@chosun.ac.kr

Keywords: strains, graphene, qubit, nanobubble

Abstract

We propose a controllable qubit in a graphene nanobubble (NB) with emergent two-level systems (TLSs) induced by pseudo-magnetic fields (PMFs). We found that double quantum dots can be created by the strain-induced PMFs of a NB, and also that their quantum states can be manipulated by either local gate potentials or the PMFs. Graphene qubits clearly exhibit avoided crossing behavior as electrical detuning, with energy splittings of about few meV. We show a remarkable tunability of our device design that allows a fine control of the Landau–Zener transition probability by strain engineering of the NB, showing half-and-half splitting at the avoided crossing point. Further, we demonstrate that the TLSs in the NB exhibit Rabi oscillations near the avoided crossing point, resulting in very fast Rabi cycles of a few ps.

Graphene is an attractive candidate for qubits due to having long relaxation and coherent times [1–4]. Since a qubit consists of two quantum states with discrete levels, the formation of graphene quantum dots (QDs) is required to construct graphene qubits. Although there have been a number of studies on graphene QDs for qubit applications [2, 5–11], the major challenge of the QD-based graphene qubit is the lack of a band gap, which does not allow for Dirac fermion confinement through electrical gating. As approaches to tackle this issue, physically etched graphene nanoconstrictions [12–16], graphene nanoribbons [17–19], and bilayer graphene [20–28] have been investigated to achieve bound states of Dirac fermions in graphene QDs. However, compared to pristine graphene, these efforts toward gap opening inevitably lead to unwanted disorders [16, 29], interrupting the precise control of the electronic states of individual QDs [28].

With the experimental confirmation of strain-induced Landau level formation in graphene [30], advancements in both theories and experimental technologies have been made, making room for an unraveling of the strain engineering of graphene [31–38]. Generation of pseudo-magnetic fields (PMFs) due to elastic strain in graphene has attracted wide research interest for the tunability of the transport properties of graphene by strain. (For details on PMFs in strained graphene, see appendix A.) In particular, there is the theoretical expectation that Dirac fermions can be localized by non-uniform PMFs [39–41]. Such a fact, namely that a nanobubble (NB) can host localized states in graphene, allows for the possibility of a new type of graphene QDs.

Another aspect of graphene is that its mechanical properties are advantageous for studying electromechanical phenomena in nanoscale devices. Graphene is not only a rigid material due to its high elastic modulus reaching up 1 TPa [42], but it is also a stretchable material with a large failure strength exceeding 100 GPa [43–45]. Since graphene exhibits a wide elastic strain regime up to 20% [44–46], researchers have noted the strain engineering of graphene for nanoelectromechanical devices with the potential ability to tune electrical properties via strain control [31, 32, 47–53]. So far, research progress in strained graphene has been focused on band gap engineering [31, 51] and valleytronics [35, 41, 54–57] while relatively overlooking the existence of localized states as a consequence of strain-induced PMFs. Here, we pay attention to a combination of strain-tunability and strain-induced localized states for graphene-based qubit applications.

In this article, we scrutinize the possibility of using NB-induced QD states in graphene for a novel type of qubit through a theoretical investigation. The graphene qubit consists of two coupled localized states inside a NB as a double QD (DQD), resulting in a two-level system (TLS). (For details on strain-induced localized states and QD formation, see appendix B.) We propose that the TLS is electrostatically tunable via local gate control, allowing for the initialization and modulation of qubits. The formation of a qubit is confirmed by the avoided crossing behavior of the TLS from resonant conductance calculations. Moreover, we show that the Landau–Zener (LZ) transition can be finely controlled by the strain of the NB. Such strain-tunability enables us to secure an exact half-and-half splitting ratio of superposed quantum states at the avoided crossing point.

Let us begin by describing the system we theoretically study in this work. We consider an armchair graphene nanoribbon in which a NB is formed at the center, modeled as a Gaussian-shaped vertical deformation:

$$z(\vec{r}) = h_0 e^{-r^2/2\sigma^2}, \tag{1}$$

where h_0 and σ represent the height and radial size of the NB. As revealed in previous studies [41, 58], the maximum PMF induced by a NB is dependent on h_0 and σ simultaneously, via $B_{\mathrm{ps,max}} \propto h_0^2/\sigma^3$. In this study, we use $h_0 = 4.2$ nm and $\sigma = 7.2$ nm, corresponding to $B_{\mathrm{ps,max}} = 248$ T. Next, we note that our system is in the quantum Hall regime since the magnetic length $l_B = \sqrt{\hbar/2eB} = 3.2$ nm is sufficiently shorter than the ribbon width $W = 76.8$ nm under a uniform external magnetic field $B = 97.8$ T. Note that for larger systems, the required strength of the magnetic field is reduced; for instance, for $W = 242$ nm, $B = 10$ T is sufficient to secure the quantum Hall regime. Additionally, let us briefly mention the magnetic field strength. A sufficiently wide energy gap between the Landau levels under a strong B leads to the advantage of energetically isolating the localized states of the DQD in a NB.

It has been previously reported that a circular NB produces a characteristic non-uniform PMF with 120° rotational symmetry [41, 56, 59]. From the tight-binding point of view, lattice deformation due to a NB is reflected in the modified hopping terms, $t_{ij} = t_0 \exp\left(-dt_{ij}\right)$ with

$$dt_{ij} = \beta\left(\frac{d_{ij}}{a_0} - 1\right), \tag{2}$$

where d_{ij} is the distance between i and j sites of graphene, t_0 is the hopping energy of unstrained graphene, $\beta \sim 3.37$, and a_0 is the lattice constant of graphene. For simplicity, we consider nearest-neighbor hoppings only.

Since the PMF is created locally at the NB location, probing it typically requires local probes like a scanning tunneling microscope, but here we use one-dimensional quantum Hall channels as a local probe. As shown in figure 1, a p–n junction is introduced in the vicinity of the NB in order to have Dirac fermions propagate throughout the NB. For a more realistic situation, we consider a gradually varying potential profile for the p–n junction rather than abrupt potential steps: $U = U_0 \tanh(x/\xi)$, leading to $\pm U_0$ in the p- or n-region. Note that we set $\xi = 30$, $a_0 \simeq 7.2$ nm, and $U_0 = \sqrt{2eB\hbar v_{\mathrm{F}}^2} \simeq 0.36$ eV, which is the spacing between the zeroth and first Landau levels.

The existence of the QD states in the NB is evidenced by Fano resonances in the conductance spectra across the p–n junction. When the Dirac fermion energy equals the energy level of a NB-induced QD, Fano resonances occur as a consequence of interference between extended states in the interface channel and localized states in the QD. Otherwise, we can simply see characteristic conductance oscillations via the valley-isospin rotation due to the PMF [41]. In this study, the coherent conductance is calculated by using S-matrix formalism based on the tight-binding approach provided in the KWANT code [60]. Furthermore, we perform time-dependent simulations on the LZ transition near the avoided crossing point using TKWANT code [61], with parameters extracted from numerical results of the conductance.

In order to discuss qubit formation, it is necessary to identify the localized states in the NB. Here, to probe the localized states, we calculated the diagonal conductance G_{D} across the p–n junction for $h_0 = 4.08$ nm by varying the NB position x_0. As shown in figure 2, the conductance exhibits characteristic oscillation as x_0 varies as a consequence of the valley-isospin rotation due to strain-induced Berry's phase [41]. Meanwhile, it is significant that there are a number of Fano resonances in the conductance spectra for different x_0, implying a number of localized states at specific locations. The Fano resonances are classified into two types: ones corresponding to single QD states and others corresponding to DQD states. It is noticeable that, for the DQD case, there is a splitting in the energies of the localized states, resulting from a superposition of the quantum states in the NB-induced DQD. Thus, like the TLS states of a DQD in a two-dimensional electron gas (2DEG) [62–64], our DQD states are able to be treated as a TLS in graphene, induced by elastic strain effects.

The existence of the superposed states indicates that there are two identical QDs in the NB and that they are coupled to each other. To see the potential for qubit application, we consider a device design with an

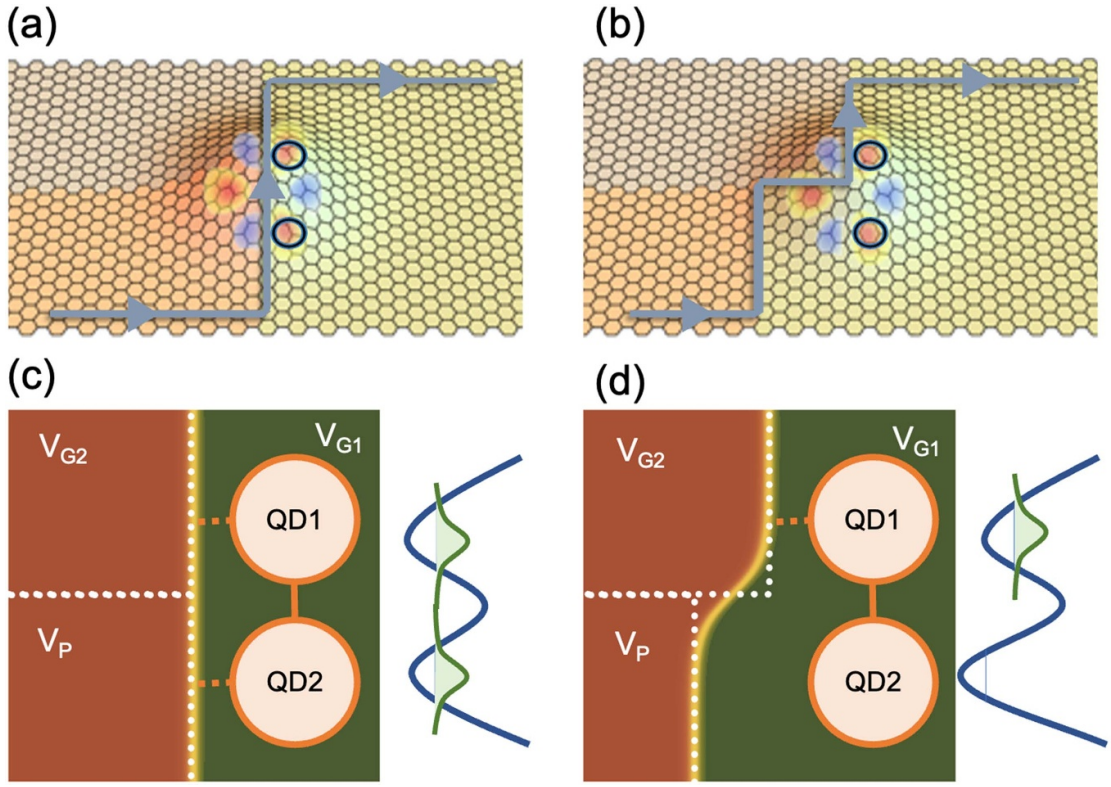

Figure 1. (a) and (b) Schematics of the system for a strain-induced DQD in graphene with symmetric and asymmetric p–n junctions. The p–n junction structures consist of three local gate electrodes: V_{G1}, V_{G2}, and V_P. A quantum Hall interface channel is created along the p–n junction interface, and the electronic states of the DQD are probed via coupling between the interface channel and the QDs. (c) For the symmetric p–n junction ($V_{G2} = V_P$), the TLS state is composed of two identical QDs. (d) For the asymmetric p–n junction ($V_{G2} \neq V_P$), the two QDs are no longer identical due to the different coupling strength between the interface channel and the QDs, so either QD1 or QD2 is occupied by an electron according to energy.

asymmetric p–n junction as a way of tuning the electronic states of the DQD. As shown in figure 1, our system is composed of three domains which can be subjected to different electrostatic potentials, and such potential profile is modeled as follows:

$$U(x,y) = U_0 \tanh\left[\frac{x + 0.5d(1+\tanh y)}{\xi}\right], \tag{3}$$

where d is the distance shift of the p–n junction via plunger gate electrode. For $d = 0$, we have the straight line of the p–n junction interface relating to the superposed states, as displayed in figure 1(c). On the other hand, as d is changed, the p–n junction interface becomes bent, and the couplings to the two QDs accordingly become asymmetric. As a result, the two QDs are no longer identical, so that the superposed states also no longer exist (see figure 1(d)).

Figure 3 shows conductance spectra in the vicinity of the superposed states for $x_0 = 27.25$ and $a_0 \simeq 6.54$ nm with varying d. As expected, for $d = 0$, we observe a clear avoided crossing behavior. At the avoided crossing point, the TLS consists of symmetric and antisymmetric superpositions of two states,

$$|\psi_+\rangle = \alpha|L\rangle + \beta|R\rangle, \qquad |\psi_-\rangle = \alpha|L\rangle - \beta|R\rangle, \tag{4}$$

where $|L\rangle$ and $|R\rangle$ indicate the ground states of QD1 and QD2, respectively. Let us notice that, at the avoided crossing point, the $|\psi_-\rangle$ state corresponds to the lower branch due to Berry's phase π of graphene.

By decreasing d from the avoided crossing point, as displayed in figure 1(d), QD2 becomes distant from the p–n junction interface, meaning that the electronic states of QD2 change in accordance with d. As a result, the TLS continuously varies from the superposed states to two individual ground states. Since the coupling between the interface channel and QD1 remains unchanged by d, the lower branch of the TLS converges on the $|L\rangle$ state such that only QD1 is allowed to be occupied by an electron, whereas the upper branch converges on $|R\rangle$ state such that only QD2 is allowed to be occupied by an electron. On the other hand, by increasing d from the avoided crossing point, the upper and lower branches encounter the $|L\rangle$ and $|R\rangle$ states, respectively.

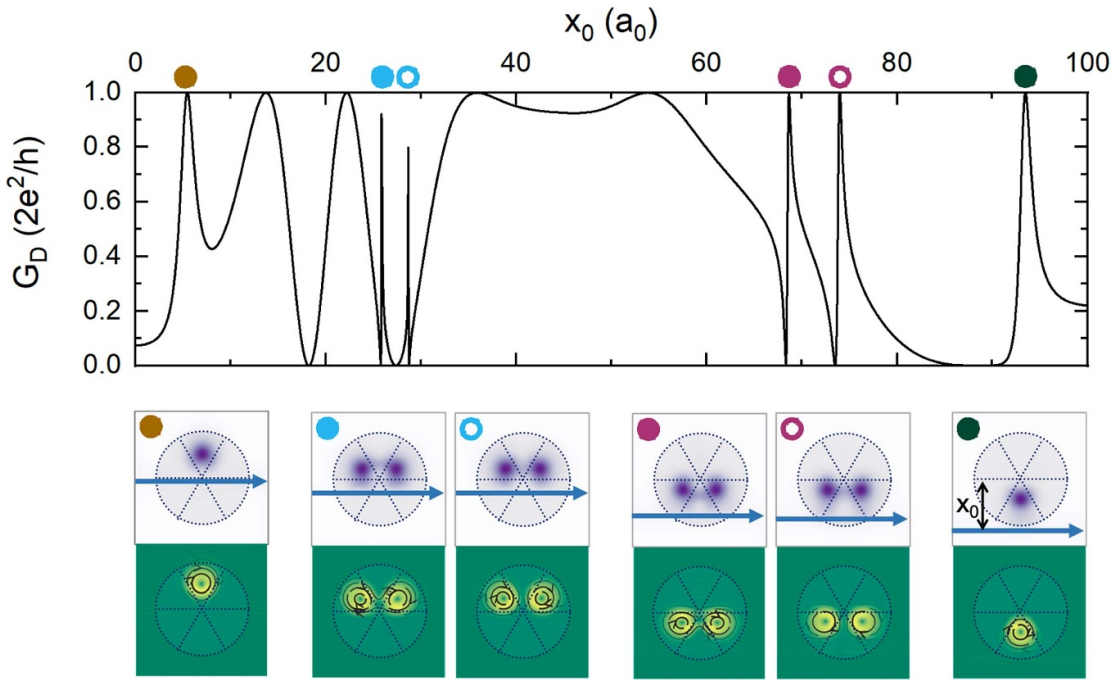

Figure 2. Identification of QD formation in the NB via Fano resonances. Top panel: conductance spectrum through the NB at the p–n junction interface as a function of the relative distance between the interface and the NB, x_0. Fano resonances are indicated by solid and open circles, corresponding to the QD states in the NB. Bottom panels: Probability and current densities for the different QD states indicated by the circle symbols with different colors. Dotted lines are eye-guides for the non-uniform PMF profile due to the NB.

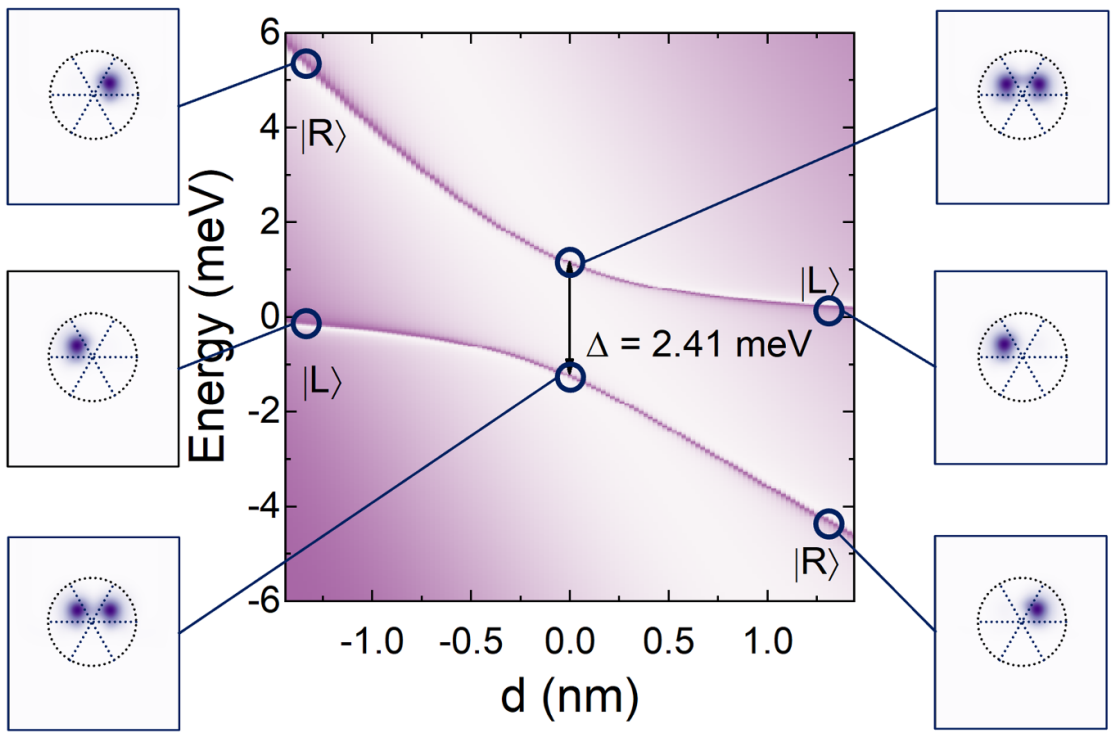

Figure 3. Avoided crossing behavior of the graphene DQD. Fano resonance lines represent the localized states of the strain-induced QD in the NB. Bright and dark colors indicate $2e^2/h$ and zero, respectively. The insets display probability density distributions of interesting cases, denoted by open circles on the color map.

Meanwhile, we figure out the energy splitting $\Delta = 2.41$ meV at the avoided crossing point, which is larger than other semiconductor QD qubits [64–67]. Such a large value of Δ corresponds to $\Omega = \Delta/h = 583.8$ GHz for the LZ transition at the avoided crossing point. One can take advantage of this

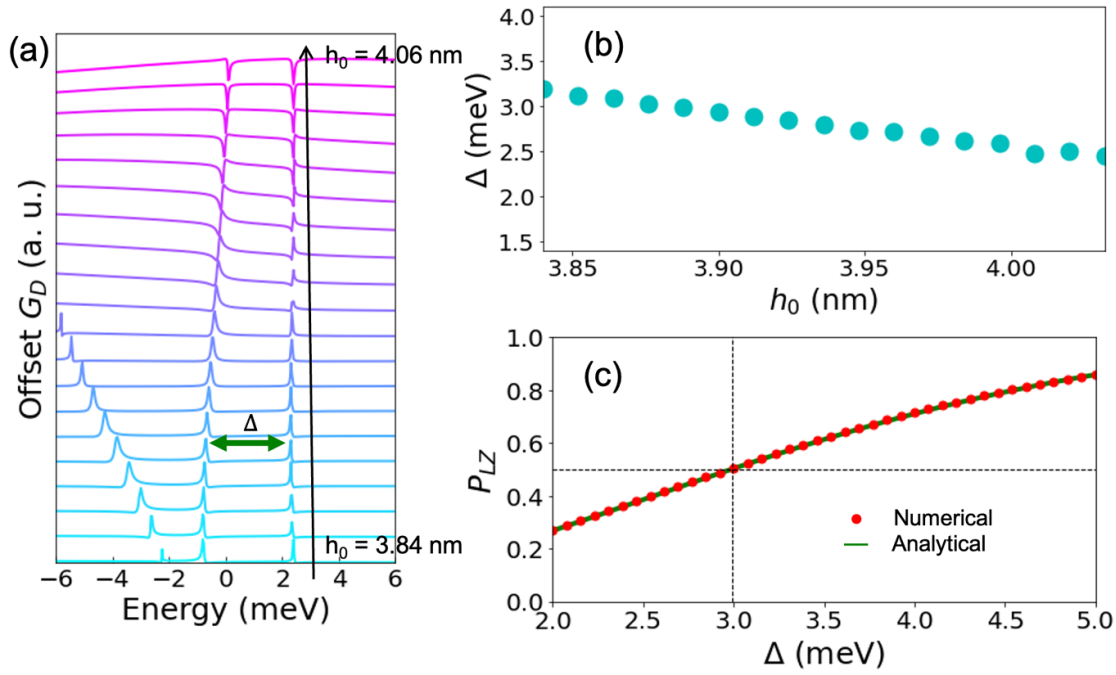

Figure 4. (a) Conductance spectra near the avoided crossing point for various h_0 values. (b) Energy splitting Δ taken from the spacing between the Fano resonances shown in (a). (c) Landau–Zener transition probabilities at the avoided crossing point as functions of Δ from both numerical and analytical calculations. Note that Δ is controllable via strain engineering of the NB.

high-frequency LZ transition, which allows for sufficient numbers of qubit operations within a finite coherence time on the order of hundreds of ns [64]. In addition, as shown in figure 2, there is another TLS in the NB with larger energy splitting $\Delta = 4.2$ meV, allowing for higher frequencies up to 1 THz.

Next, we move our focus to the tunability of the LZ transition near the avoided crossing point of the graphene DQD. As each TLS approaches the avoided crossing point, coupling between the two QDs begins increasing, so that the quantum state undergoes the LZ transition with the transition probability:

$$P_{\mathrm{LZ}} = 1 - e^{-\frac{\pi\Delta^2}{2\hbar v}}, \tag{5}$$

where Δ is the energy splitting at the avoided crossing point and v is the sweep speed of an energy evolution for qubit manipulation. Since the energy splitting Δ is associated with the coupling between the QDs, it is obvious to expect that Δ is not constant but variable as the PMF strength changes. In fact, unless the circular shape of the NB is deformed, the characteristic profile of the PMF is unchanged but the strength of the PMF is changed by either h_0 or σ [41]. Here, for simplicity, we focus on the effects of h_0 to see how Δ changes as the PMF strength varies. Figure 4 exhibits a clear dependence of Δ on h_0. The energy splitting Δ becomes smaller for stronger PMFs, i.e. larger h_0 values. This behavior is intuitively understood with the following: a stronger PMF brings about a stronger confinement of Dirac fermions, which weakens the coupling between the QDs, which in turn results in a smaller energy splitting at the avoided crossing point.

Due to the strain-tunable energy splitting of the graphene DQD, it is straightforward to expect that the LZ transition can also be tuned by strain engineering. In particular, obtaining a half probability of the LZ transition is significant for quantum interference technology, like LZ–Stückelberg interferometry. From equation (5), we find the required energy splitting for $P_{\mathrm{LZ}} = 0.5$ through

$$\Delta_h = \sqrt{\frac{2\ln 2 a\hbar\omega}{\pi}}, \tag{6}$$

assuming that a time-dependent perturbation for qubit operation is a part of a sinusoidal time-evolution of each TLS with amplitude a and frequency ω. Let us briefly notice that $a \sim 0.1$ V and $\omega \sim 100$ GHz are practical values for graphene-based electronic device operation, so $a\omega$ is on the order of 10 eV·GHz. For $\Delta_h = 2.41$ meV, we need $a\omega = 2$ eV·GHz. Meanwhile, in order to see how the LZ transition probability is finely tunable, we perform a numerical calculation of one time-dependent TLS for a different value $a\omega = 3.03$ eV·GHz. The resulting LZ transition probability as a function of Δ is displayed in figure 4(c). We find $P_{\mathrm{LZ}} = 0.5$ when $\Delta = 3$ eV, which corresponds to $h_0 = 3.89$ nm. If we consider a Δ initially set to 2.41 eV with $h_0 = 4.06$ nm, then a 50% LZ transition probability is acquired by finely tuning h_0 as much as 0.17 nm.

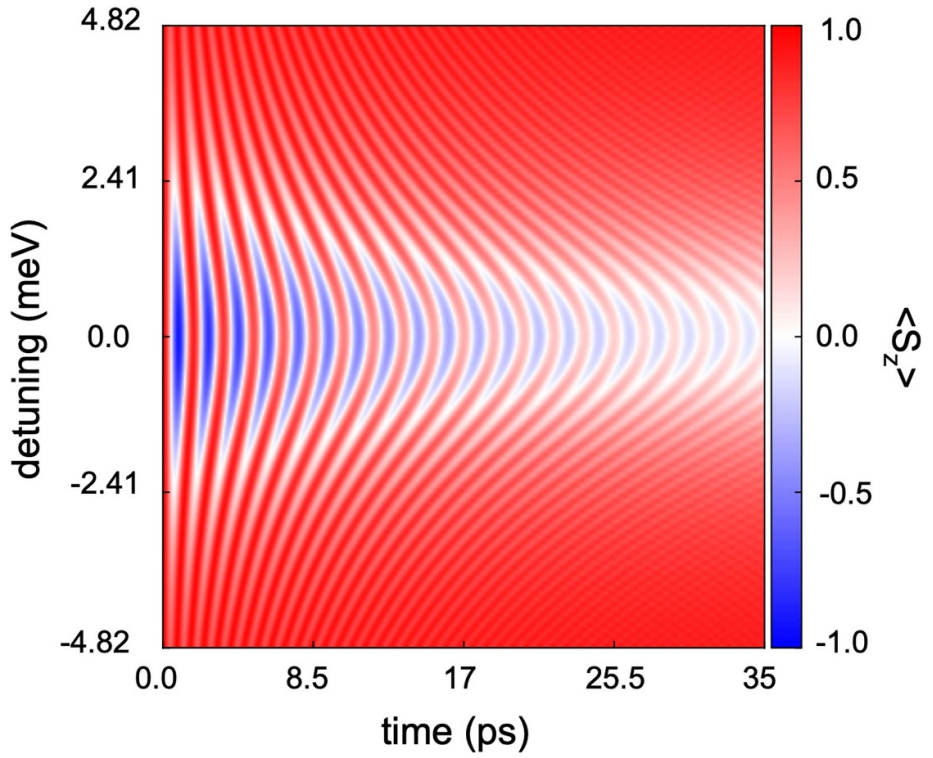

Figure 5. Rabi oscillation map showing S_z expectation values defined in the concept of a Bloch sphere. $\langle S_z \rangle = 1$ indicates that the TLS resides in the $|\psi_+\rangle$ state, i.e. an excited state. The zero detuning implies that the two QDs in the NB are set to be identical for the TLS formation at the avoided crossing point.

Furthermore, we also examine the potential of our DQD for graphene qubit applications by investigating the dynamics of the quantum states at the avoided crossing point. Since the strain-induced DQD in the NB has weak but non-negligible coupling with the interface channel at the p–n junction, we consider that the quantum states of the TLS undergo dissipative interactions with the surroundings as a thermal bath. In order to describe such a dissipative dynamics of the TLS, we introduce the following effective Hamiltonian with the energy splitting Δ at the avoided crossing point,

$$H = \frac{\varepsilon}{2}(\sigma_0 + \sigma_z) + \frac{\Delta}{2}\sigma_x, \tag{7}$$

where ε is the detuning energy. The dynamics of the quantum states with dissipative interaction is governed by the Lindblad equation:

$$\frac{\mathrm{d}\rho}{\mathrm{d}t} = -\frac{i}{\hbar}[H,\rho] + \left(\Gamma_\varphi \mathcal{D}_{\sigma_z}[\rho] + \Gamma(1-\overline{n})\mathcal{D}_{\sigma_-}[\rho] + \Gamma\overline{n}\mathcal{D}_{\sigma_+}[\rho]\right), \tag{8}$$

where $\mathcal{D}_L[\rho] = L\rho L^\dagger - \frac{1}{2}\{L^\dagger L, \rho\}$ with $\{A,B\}$ being an anti-commutator between two operators A, B, $\overline{n}$ is the Fermi–Dirac distribution at temperature T of the thermal bath, Γ_φ is the dephasing rate of the quantum states, and Γ is the relaxation rate as a result of the coupling between the DQD and the interface channel [68]. Note that in the absence of Γ_φ and Γ, the TLS becomes fully coherent. Due to the long phase relaxation time of graphene [2, 16, 69, 70], we assume that the dynamics of the quantum states is dominated by the dissipative coupling with the thermal bath, i.e. $\Gamma \gg \Gamma_\varphi$. In this study, the relaxation rate due to the dissipation is extracted from the numerical results of the Fano resonances, $\Gamma \simeq 86$ GHz. Numerically solving equation (8), we can obtain the expectation values of σ_z. Figure 5 shows clear Rabi oscillations with zero detuning $\varepsilon = 0$, undergoing attenuation as a consequence of the dissipative coupling. From figure 5, the period of the Rabi cycle is estimated to be 1.75 ps; this value is in good agreement with $\Omega = \Delta/h = 583.8\,\mathrm{GHz} \simeq (1.75\,\mathrm{ps})^{-1}$. Lastly, let us notice that the ultra-fast response of Dirac fermions to external electric fields (>100 GHz [71, 72]) supports such a fast operation frequency of our strain-induced qubit.

In summary, we have found tunable TLSs in graphene by demonstrating the formation of a DQD due to the PMF induced by elastic strain from a NB. The strain-induced graphene DQD can exhibit an energy splitting into two levels via symmetric and antisymmetric superpositions of localized states in the two QDs. Considering p–n junctions in the quantum Hall regime, we have shown that the quantum states of the TLS

in the graphene DQD can be manipulated via gate control. Our DQD exhibits clear avoided crossing behavior, resulting in 2.41 and 4.2 meV energy splittings. We have also revealed that the LZ transition can be finely tuned—by means of strain control—for a pure half-and-half splitting of the quantum states at the avoided crossing point. Further, we have demonstrated that the dynamics of the quantum states near the avoided crossing point exhibits clear Rabi oscillations. The few-ps Rabi cycles make our graphene DQD promising for ultra-fast qubit operation.

By suggesting a novel way of forming QD devices in graphene, our findings have implications for research on QDs. The strain-induced graphene DQD in a NB is advantageous for the following reasons: the *strain-tunability* of quantum states, and the ultra-fast operation within the long coherence time of graphene, and exploiting pristine properties of monolayer graphene without a substantial reduction in quantum coherence. Furthermore, our finding of the strain-tunable two-level splittings may enable high operation frequencies to be tuned down via strain engineering. In conclusion, we expect that our results may inaugurate strain-engineered qubits, exploiting the properties of pristine graphene.

Data availability statement

The data cannot be made publicly available upon publication because the cost of preparing, depositing and hosting the data would be prohibitive within the terms of this research project. The data that support the findings of this study are available upon reasonable request from the authors.

Acknowledgments

This work was supported by funds from the National Research Foundation of Korea (NRF-2022R1F1A1065365), Project Code IBS-R024-D1. The authors also acknowledge the support from the Korea Institute for Advanced Study (KIAS). The authors thank Mr Rasmussen at RECON for the professional English editing.

Appendix A. Pseudo-magnetic fields in strained graphene

In the tight-binding model with nearest-neighbor hopping only, the discrete Hamiltonian of graphene reads

$$H = -\sum_{\langle i,j\rangle}\left(t_{ij}a_i^\dagger b_j + h.c.\right), \tag{9}$$

where $a_i^\dagger$ (a_i) and $b_i^\dagger$ (b_i) indicate creation(annihilation) operators at each sublattice (denoted by A and B) in the ith unit cell. Since hopping is restricted between nearest neighbors, there are three allowed hoppings from one A site to B sites, and these hoppings are defined by the following vectors:

$$\vec{\delta}_1 = a_0\,(0,1)\,, \qquad \vec{\delta}_2 = a_0\left(\frac{1}{2},-\frac{\sqrt{3}}{2}\right), \qquad \vec{\delta}_3 = a_0\left(-\frac{1}{2},-\frac{\sqrt{3}}{2}\right), \tag{10}$$

where a_0 is the distance between adjacent A and B sites of graphene.

Through a Fourier transform, the creation operator is written as

$$a_i^\dagger = \frac{1}{\sqrt{N/2}}\sum_k e^{i\vec{k}\cdot\vec{r}_i}a_k^\dagger, \tag{11}$$

where N is the number of sites of the system. Thus, the tight-binding Hamiltonian in momentum space is written as

$$H = -\sum_{k,k'}\sum_{n=1}^{3}\left[t_i\left(\vec{\delta}_n\right)e^{-i\left(\vec{k}'-\vec{k}\right)\cdot\vec{r}_i}e^{-i\vec{k}'\cdot\vec{\delta}_n}a_k^\dagger b_{k'} + h.c.\right] \tag{12}$$

between $\vec{k}$ and $\vec{k}'$ points, in general. Using orthogonality, the Hamiltonian reads

$$H = -\sum_{k}\sum_{n=1}^{3}\left[t_0 e^{-i\vec{k}\cdot\vec{\delta}_n}a_k^\dagger b_k + h.c.\right], \tag{13}$$

where $t_0 = 3$ eV.

For strained graphene, the vectors $\vec{\delta}_n$ change according to the modified distance between lattice sites. In this case, the tight-binding Hamiltonian becomes

$$H = -\sum_k \sum_{n=1}^{3} \left[t_0 e^{-i\vec{k}\cdot\left(\vec{\delta}_n + \vec{\varepsilon}_n\right)} a_k^\dagger b_k + h.c. \right] = -\sum_k \sum_{n=1}^{3} \left[t e^{-i\vec{k}\cdot\vec{\delta}_n} a_k^\dagger b_k + h.c. \right], \tag{14}$$

where $\vec{\varepsilon}_n$ is the modified carbon–carbon distance, and the modified hopping terms are given by

$$t = t_0 e^{-i\vec{k}\cdot\vec{\epsilon}_n}. \tag{15}$$

Therefore, Dirac fermions acquire an additional phase while moving through a strained graphene sheet. Such an acquired phase can be assumed to be a consequence of emergent gauge fields in an unstrained graphene sheet. In this case, the hopping terms are rewritten as

$$t = t_0 e^{-i\frac{e}{\hbar}\int \vec{A}_{ps}\cdot \mathrm{d}\vec{r}}. \tag{16}$$

Now, the definition of a pseudo-magnetic field (PMF) can be given as $\vec{B}_{\mathrm{ps}} = \vec{\nabla} \times \vec{A}_{\mathrm{ps}}$, mimicking the Maxwell equation for a real magnetic field.

Appendix B. Strain-induced localized states and quantum dot formation

In elastic theory, the strain tensor is given by

$$u_{ij} = \frac{1}{2}\left(\frac{\partial u_i}{\partial x_j} + \frac{\partial u_j}{\partial x_i} + \frac{\partial u_k}{\partial x_i}\frac{\partial u_k}{\partial x_j} \right), \tag{17}$$

where $\vec{u}$ is the displacement vector. For simplicity, we assume that displacement due to a nanobubble (NB) in graphene occurs in the vertical direction, i.e. $u_x = u_y = 0$. In this case, the strain tensor is calculated as follows:

$$u_{xx} = \frac{h_0^2}{2\sigma^4} x^2 e^{-\left(x^2+y^2\right)/\sigma^2}, \quad u_{yy} = \frac{h_0^2}{2\sigma^4} y^2 e^{-\left(x^2+y^2\right)/\sigma^2}, \quad u_{xy} = \frac{h_0^2}{2\sigma^4} xy e^{-\left(x^2+y^2\right)/\sigma^2}. \tag{18}$$

From the strain tensor, a gauge field in strained graphene is derived by

$$\begin{pmatrix} A_{\mathrm{ps},x} \\ A_{\mathrm{ps},y} \end{pmatrix} = \nu \frac{\hbar\beta}{e a_0} \begin{pmatrix} \cos 3\Omega & \sin 3\Omega \\ -\sin 3\Omega & \cos 3\Omega \end{pmatrix} \begin{pmatrix} u_{xx} - u_{yy} \\ -2u_{xy} \end{pmatrix}, \tag{19}$$

where $\nu = \pm 1$ for different valley degrees of freedom, $\beta = -C(\partial \ln t)/(\partial \ln a_0) = 3.37$, and $\Omega = 0$ or $\pi/2$ for the armchair or zigzag direction, respectively. In this work, we put $\Omega = \pi/2$, and for the K valley, the resulting gauge field reads

$$A_{\mathrm{ps},x} = -\nu \frac{\hbar\beta}{e a_0} \frac{h_0^2}{\sigma^4} xy e^{-\left(x^2+y^2\right)/\sigma^2}, \quad A_{\mathrm{ps},y} = \nu \frac{\hbar\beta}{2e a_0} \frac{h_0^2}{\sigma^4} \left(x^2 - y^2\right) e^{-\left(x^2+y^2\right)/\sigma^2}. \tag{20}$$

Meanwhile, it is convenient to use a polar coordinate system, and the gauge field in polar coordinates is given by

$$\vec{A}_{\mathrm{ps}} = \nu \frac{\hbar\beta}{2e a_0} \frac{h_0^2}{\sigma^4} r^2 e^{-r^2/\sigma^2} \left(\cos 3\theta \hat{r} - \sin 3\theta \hat{\theta} \right). \tag{21}$$

Now, the pseudo-magnetic field (PMF) is derived as

$$\vec{B}_{\mathrm{ps}} = \vec{\nabla} \times \vec{A}_{\mathrm{ps}} = \frac{1}{r}\left[\frac{\partial}{\partial r}\left(r A_{\mathrm{ps},\theta} \right) - \frac{\partial A_{\mathrm{ps},r}}{\partial \theta} \right] \hat{z} = \frac{h_0^2}{\sigma^6} r^3 e^{-r^2/\sigma^2} \sin 3\theta \hat{z}. \tag{22}$$

The spatial profile of the PMF due to a NB is plotted in figure 6. The characteristic length in systems under magnetic fields is determined by the magnetic length $l_B = \sqrt{\hbar/eB}$, and the radius is also proportional to l_B when considering semi-classical cyclotron motion. Thus, for a sufficiently strong B, localized states can be created by the formation of a cyclotron motion around the maximum/minimum positions of B. This is why localized states are found for large h_0 with a given σ, as discussed in our preliminary work [41].

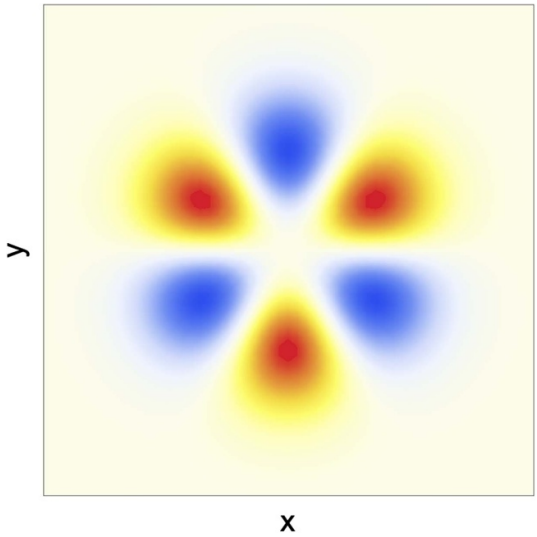

Figure 6. PMF profile due to a nanobubble in graphene. Blue and red colors indicate negative and positive field strengths, respectively.

The emergence of the strain-induced localized states in a NB can also be interpreted by the effective potential. Under a homogeneous external magnetic field, the Dirac equation of graphene with a NB at a p–n junction reads

$$v_{\mathrm{F}}\begin{pmatrix} 0 & \Pi_x - i\Pi_y & 0 & 0 \\ \Pi_x + i\Pi_y & 0 & 0 & 0 \\ 0 & 0 & 0 & -\Pi_x - i\Pi_y \\ 0 & 0 & -\Pi_x + i\Pi_y & 0 \end{pmatrix}\begin{pmatrix} \psi_A \\ \psi_B \\ \psi'_A \\ \psi'_B \end{pmatrix} = [E - U(x)]\begin{pmatrix} \psi_A \\ \psi_B \\ \psi'_A \\ \psi'_B \end{pmatrix}, \tag{23}$$

where $\vec{\Pi} = \vec{p} + \nu e\left(\vec{A} + \vec{A}_{\mathrm{ps}}\right)$ with $\nu = \pm 1$ for different valleys. Here, $\vec{A}$ and $\vec{A}_{\mathrm{ps}}$ are a magnetic vector potential and a strain-induced gauge field related to a real and a pseudo-magnetic field via $\vec{B} = \vec{\nabla} \times \vec{A}$ and $\vec{B}_{\mathrm{ps}} = \vec{\nabla} \times \vec{A}_{\mathrm{ps}}$, respectively. For $\vec{B} = B\hat{z}$, the magnetic vector potential is given as

$$\vec{A} = -\frac{1}{2}Br\hat{\theta}, \tag{24}$$

and the potential energy for the p–n junction is formulated by

$$U(x) = U_0 \tanh\frac{x}{\xi}, \tag{25}$$

where ξ is a parameter to determine the steepness of the p–n junction. By decoupling the above Dirac equation, we obtain the following Schrödinger-like equations:

$$\left[\frac{E - U(x)}{v_{\mathrm{F}}}\right]^2\begin{pmatrix} \psi_A \\ \psi_B \end{pmatrix} = \begin{pmatrix} \Pi^2 + e\hbar\left[B_{\mathrm{ps}}(r) - B\right] & 0 \\ 0 & \Pi^2 - e\hbar\left[B_{\mathrm{ps}}(r) - B(r)\right] \end{pmatrix}\begin{pmatrix} \psi_A \\ \psi_B \end{pmatrix} \tag{26}$$

$$\left[\frac{E - U(x)}{v_{\mathrm{F}}}\right]^2\begin{pmatrix} \psi'_A \\ \psi'_B \end{pmatrix} = \begin{pmatrix} \Pi'^2 + e\hbar\left[B_{\mathrm{ps}}(r) + B\right] & 0 \\ 0 & \Pi'^2 - e\hbar\left[B_{\mathrm{ps}}(r) + B(r)\right] \end{pmatrix}\begin{pmatrix} \psi'_A \\ \psi'_B \end{pmatrix}. \tag{27}$$

The properties of the bound states in a NB are analyzed by introducing the effective potential:

$$U_{\mathrm{eff}} = v_{\mathrm{F}}^2 e\hbar\left[\mu B_{\mathrm{ps}}(r) - \nu\mu B\tau_z \otimes \sigma_z\right] - [E - U(r,\theta)]^2, \tag{28}$$

where $\nu = \pm 1$ for different valleys K and K' and $\mu = \pm 1$ for different sublattices A and B, respectively.

The effective potential for $\nu = 1$ and $\mu = 1$ is displayed in figure 7. By qualitative analysis, bound states can be found to be near the local minima. In the absence of the p–n junction, there are three local minima, as if a triple quantum dot is created. Indeed, as reported in a previous study on the electronic states in a graphene NB [73], there are triply degenerate bound states, and this degeneracy is lifted by the presence of a real magnetic field, resulting in energy splittings into six levels. On the other hand, with the p–n junction

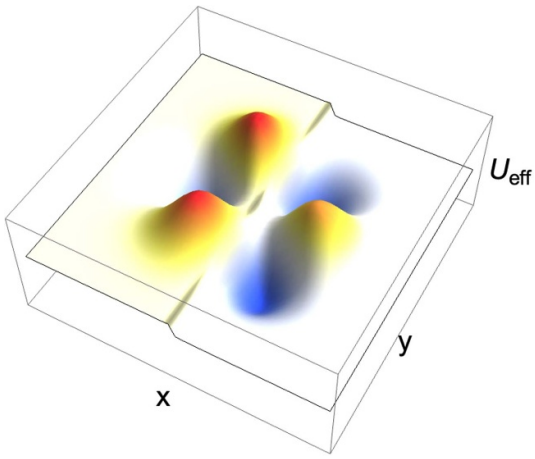

Figure 7. Effective double-well potential due to a nanobubble in graphene with a p–n junction for the K valley and A sublattice.

potential, the left half of U_{eff} along the x-axis is lowered while the right half is elevated. As a result, two local minima in one half are shifted toward lower energy, whereas one local minima in the other half is shifted toward higher energy. Therefore, one can consider that there emerges a DQD near the p–n junction interface.

ORCID iD

Nojoon Myoung https://orcid.org/0000-0003-2344-5793

References

[1] Huertas-Hernando D, Guinea F and Brataas A 2006 *Phys. Rev.* B **74** 155426
[2] Trauzettel B, Bulaev D V, Loss D and Burkard G 2007 *Nat. Phys.* **3** 192–6
[3] Borysenko K M, Mullen J T, Barry E A, Paul S, Semenov Y G, Zavada J M, Buongiorno Nardelli M and Kim K W 2010 *Phys. Rev.* B **81** 121412(R)
[4] Han W, McCreary K M, Pi K, Wang W H, Li Y, Wen H, Chen J and Kawakami R K 2012 *J. Magn. Magn. Mater.* **324** 369–81
[5] Pedersen T G, Flindt C, Pedersen J, Mortensen N A, Jauho A P and Pedersen K 2008 *Phys. Rev. Lett.* **100** 136804
[6] Recher P, Nilsson J, Burkard G and Trauzettel B 2009 *Phys. Rev.* B **79** 085407
[7] Recher P and Trauzettel B 2010 *Nanotechnology* **21** 302001
[8] Wu G Y and Lue N-Y 2012 *Phys. Rev.* B **86** 045456
[9] Wang C, Shen W W, Mi S C, Zhang Y and Wang T J 2015 *Sci. Bull.* **60** 2016–21
[10] Chen C C and Chang Y C 2015 *Phys. Rev.* B **92** 245406
[11] Dong Q, Yin X and Liu C 2021 *Physica* E **127** 114555
[12] Güttinger J, Stampfer C, Hellmüller S, Molitor F, Ihn T and Ensslin K 2008 *Appl. Phys. Lett.* **93** 212102
[13] Güttinger J, Stampfer C, Frey T, Ihn T and Ensslin K 2009 *Phys. Status Solidi* b **246** 2553–7
[14] Ihn T *et al* 2010 *Mater. Today* **13** 44–50
[15] Güttinger J, Molitor F, Stampfer C, Schnez S, Jacobsen A, Dröscher S, Ihn T and Ensslin K 2012 *Rep. Prog. Phys.* **75** 126502
[16] Engels S, Epping A, Volk C, Korte S, Voigtländer B, Watanabe K, Taniguchi T, Trellenkamp S and Stampfer C 2013 *Appl. Phys. Lett.* **103** 073113
[17] Stampfer C, Güttinger J, Hellmüller S, Molitor F, Ensslin K and Ihn T 2009 *Phys. Rev. Lett.* **102** 056403
[18] Gallagher P, Tood K and Goldhaber-Gordon D 2010 *Phys. Rev.* B **81** 115409
[19] Wang S, Kharche N, Costa Girão E C, Feng X, Müllen K, Meunier V, Fasel R and Ruffieux P 2017 *Nano Lett.* **17** 4277–83
[20] Pereira J M, Vasilopoulos P and Peeters F M 2007 *Nano Lett.* **7** 946–9
[21] da Costa D R, Zarenia M, Chaves A, Farias G A and Peeters F M 2014 *Carbon* **78** 392–440
[22] da Costa D R, Zarenia M, Chaves A, Farias G A and Peeters F M 2015 *Phys. Rev.* B **92** 115437
[23] da Costa D R, Zarenia M, Chaves A, Farias G A and Peeters F M 2016 *Phys. Rev.* B **93** 085401
[24] Velasco J J *et al* 2018 *Nano Lett.* **18** 5104–10
[25] Eich M *et al* 2018 *Phys. Rev.* X **8** 031023
[26] Kurzmann A *et al* 2019 *Phys. Rev. Lett.* **123** 026803
[27] Kurzmann A *et al* 2019 *Nano Lett.* **19** 5216–21
[28] Banszerus L *et al* 2020 *Nano Lett.* **20** 7709–15
[29] Bischoff D, Krahenmann T, Dröscher S, Gruner M A, Barraud C, Ihn T and Ensslin K 2012 *Appl. Phys. Lett.* **101** 203103
[30] Levy N, Burke S A, Meaker K L, Panlasigui M, Zettl A, Guinea F, Castro Neto A H and Crommie M F 2010 *Science* **329** 544–7
[31] Pereira V M and Castro Neto A H 2009 *Phys. Rev. Lett.* **103** 046801
[32] Guinea F, Katsnelson M I and Geim A K 2010 *Nat. Phys.* **6** 30–33
[33] Guinea F, Geim A K, Katsnelson M I and Novoselov K S 2010 *Phys. Rev.* B **81** 035408
[34] Vozmediano M, Katsnelson M and Guinea F 2010 *Phys. Rep.* **496** 109–48
[35] Low T and Guinea F 2010 *Nano Lett.* **10** 3551–4
[36] Klimov N N, Jung S, Zhu S, Li T, Wright C A, Solares S D, Newell D B, Zhitenev N B and Stroscio J A 2012 *Science* **336** 1557–61

[37] Xu P et al 2012 Phys. Rev. B 85 121406(R)
[38] Zhu S, Huang Y, Klimov N N, Newell D B, Zhitenev N B, Stroscio J A, Solares S D and Li T 2014 Phys. Rev. B 90 075426
[39] Qi Z, Kitt A L, Park H S, Pereira V M, Campbell D K and Castro Neto A H 2014 Phys. Rev. B 90 125419
[40] Bahamon D A, Qi Z, Park H S, Pereira V M and Campbell D K 2015 Nanoscale 7 15300–9
[41] Myoung N, Choi H and Park H C 2020 Carbon 157 578–82
[42] Lee C, Wei X, Kysar J W and Hone J 2008 Science 321 385–7
[43] Liu F, Ming P and Li J 2007 Phys. Rev. B 76 064120
[44] Cadelano E, Palla P L, Giordano S and Colombo L 2009 Phys. Rev. Lett. 102 235502
[45] Zhao H, Min K and Aluru N R 2009 Nano Lett. 9 3012–15
[46] Wei X, Fragneaud B, Marianetti C A and Kysar J W 2009 Phys. Rev. B 80 205407
[47] Choi S M, Jhi S H and Son Y W 2010 Phys. Rev. B 81 081407(R)
[48] Cocco G, Cadelano E and Colombo L 2010 Phys. Rev. B 81 241412(R)
[49] Gui G, Li J and Zhong J 2008 Phys. Rev. B 78 075435
[50] Mohr M, Papagelis K, Maultzsch J and Thomsen C 2009 Phys. Rev. B 80 205410
[51] Ni Z H, Yu T, Lu Y H, Wang Y, Feng Y P and Shen Z X 2008 Nano Lett. 2 2301–5
[52] Fu X W et al 2011 Appl. Phys. Lett. 99 213107
[53] Zhao J, Wang G, Yang R, Lu X, Cheng M, He C, Xie G, Meng J, Shi D and Zhang G 2015 ACS Nano 9 1622–9
[54] Hsu C C, Teague M L, Wang J Q and Yeh N C 2020 Sci. Adv. 6 eaat9488
[55] Wu Z, Zhai F, Peeters F M, Xu H Q and Chang K 2011 Phys. Rev. Lett. 106 176802
[56] Georgi A et al 2017 Nano Lett. 17 2240–5
[57] Zhai F, Zhao X, Chang K and Xu H Q 2010 Phys. Rev. B 82 115442
[58] Milovanović S and Peeters F 2016 J. Phys.: Condens. Matter 29 075601
[59] Moldovan D, Masir M R and Peeters F 2013 Phys. Rev. B 88 035446
[60] Groth C W, Wimmer M, Akhmerov A R and Waintal X 2014 New J. Phys. 16 063065
[61] Kloss T, Weston J, Gaury B, Rossignol B, Groth C and Waintal X 2020 New J. Phys. 23 023025
[62] Hayashi T, Fujisawa T, Cheong H D, Jeong Y H and Hirayama Y 2003 Phys. Rev. Lett. 91 226804
[63] Petta J R, Johnson A C, Marcus C M, Hanson M P and Gossard A C 2004 Phys. Rev. Lett. 93 186802
[64] Gorman J, Hasko D G and Williams D A 2005 Phys. Rev. Lett. 95 090502
[65] Goswami S et al 2007 Nat. Phys. 3 41–45
[66] Borselli M G et al 2011 Appl. Phys. Lett. 98 123118
[67] Nichol J M, Orona L A, Harvey S P, Fallahi S, Gardner G C, Manfra M J and Yacoby A 2017 npj Quantum Inf. 3 3
[68] Breuer H P and Petruccione F 2002 The Theory of Open Quantum Systems (Oxford: Oxford University Press)
[69] Coish W A and Loss D 2004 Phys. Rev. B 70 195340
[70] Volk C, Neumann C, Kazarski S, Fringes S, Engels S, Haupt F, Müller A and Stampfer C 2013 Nat. Commun. 4 1–6
[71] Xia F, Mueller T, Lin Y, Valdes-Garcia A and Avouris P 2009 Nat. Nanotechnol. 4 839–43
[72] Liu M, Yin X, Ulin-Avila E, Geng B, Zentgraf T, Ju L, Wang F and Zhang X 2011 Nature 474 64–67
[73] Park H C, Son M, Lee S J and Myoung N 2021 J. Kor. Phys. Soc. 78 1208–14